

Available online at www.sciencedirect.com

ScienceDirect

www.elsevier.com/locate/jes

JES
JOURNAL OF
ENVIRONMENTAL
SCIENCES
www.jesc.ac.cn

Synthesis, characterization, and photocatalytic activity of porous La–N–co-doped TiO₂ nanotubes for gaseous chlorobenzene oxidation

Zhuowei Cheng, Zhiqi Gu, Jianmeng Chen*, Jianming Yu, Lingjun Zhou

College of Biological and Environmental Engineering, Zhejiang University of Technology, Hangzhou 310014, China

ARTICLE INFO

Article history:

Received 10 July 2015

Revised 2 September 2015

Accepted 8 September 2015

Available online 16 March 2016

Keywords:

Photocatalysis

La/N–TiO₂

Chlorobenzene

Conversion efficiency

Kinetic analysis

ABSTRACT

The photocatalytic oxidation of gaseous chlorobenzene (CB) by the 365 nm-induced photocatalyst La/N–TiO₂, synthesized via a sol–gel and hydrothermal method, was evaluated. Response surface methodology (RSM) was used to model and optimize the conditions for synthesis of the photocatalyst. The optimal photocatalyst was 1.2La/0.5N–TiO₂ (0.5) and the effects of La/N on crystalline structure, particle morphology, surface element content, and other structural characteristics were investigated by XRD (X-ray diffraction), TEM (Transmission Electron Microscopy), FTIR (Fourier transform infrared spectroscopy), UV–vis (Ultraviolet–visible spectroscopy), and BET (Brunauer Emmett Teller). Greater surface area and smaller particle size were produced with the co-doped TiO₂ nanotubes than with reference TiO₂. The removal of CB was effective when performed using the synthesized photocatalyst, though it was less efficient at higher initial CB concentrations. Various modified Langmuir–Hinshelwood kinetic models involving the adsorption of chlorobenzene and water on different active sites were evaluated. Fitting results suggested that competitive adsorption caused by water molecules could not be neglected, especially for environments with high relative humidity. The reaction intermediates found after GC–MS (Gas chromatography–mass spectrometry) analysis indicated that most were soluble, low-toxicity, or both. The results demonstrated that the prepared photocatalyst had high activity for VOC (volatile organic compounds) conversion and may be used as a pretreatment prior to biopurification.

© 2016 The Research Center for Eco-Environmental Sciences, Chinese Academy of Sciences.

Published by Elsevier B.V.

Introduction

The continual release of volatile organic compounds (VOCs) into the atmosphere from a variety of sources (i.e., industry, transportation and household products) has resulted in the gradual degradation of the environment. New and stricter enforcement of new emission regulations has motivated efforts at reducing and preventing harmful emissions. Some conventional treatments for this environmental problem include biofiltration, which is user-friendly and affordable and has been used

successfully in the removal of VOCs, especially those with low toxicity or hydrophilic components (Kennes and Veiga, 2010). Among VOCs, chlorobenzene is listed by the US Environmental Protection Agency as a priority pollutant. It cannot be removed by biofiltration because it is bio-refractory and hydrophobic (Zhang et al., 2012). In order to develop more cost-effective methods of removing pollutants from water, research focused on combined treatments with biofiltration has received increasing attention in recent years (Leethochawalit et al., 2001; Rene et al., 2012; Mondal et al., 2014). It has been predicted that specific pretreatments,

* Corresponding author. E-mail: jchen@zjut.edu.cn (Jianmeng Chen).

such as photolysis, photocatalysis, and other advanced oxidation processes, may improve the biofiltration influent waste stream and render removal more efficient (Wei et al., 2010; Yu et al., 2014).

In the past two decades, heterogeneous photocatalytic oxidation (PCO) has been developed and used to remove VOCs (Mo et al., 2009). Due to its high activity, long-term stability, lack of toxicity, and low cost, titanium dioxide (TiO_2) has been used as a semiconductor-based photocatalyst (Adjimi et al., 2014). However, there are some inherent disadvantages that limit the use of conventional TiO_2 , including its relatively short excitation wavelength ($<387\text{ nm}$), which falls into the UV region, and relatively high recombination ratio of photogenerated electron-hole pairs (Yu and Brouwers, 2009; Kim and Choi, 2010; Wu et al., 2010a, 2010b; Wang et al., 2011, 2012).

Overcoming these limitations has been of continuing interest to the scientific community. Elemental doping can modify the properties of TiO_2 , enhance the separation of photogenerated electron-hole pairs, and increase the adsorption range. Nitrogen, carbon, sulfur, and fluoride are non-metals that can be incorporated into the TiO_2 structure to increase photocatalytic activity at longer wavelengths (Zhang et al., 2006). Non-metal doped TiO_2 (such as nitrogen-doped TiO_2 ; N- TiO_2) has been used for indoor air purification with VOCs that are easily degradable and present only at low concentrations (Qu et al., 2009). Some researchers have indicated that metal doping could extend the adsorption spectrum and significantly delay the recombination of electron-hole pairs (Pelaez et al., 2012). However, they have also reported that the structure of these prepared catalysts does not improve photocatalytic efficiency (including surface adsorption) (Tseng et al., 2009).

Co-doping a metal with non-metal species into TiO_2 has been proposed (Li et al., 2008; Wu et al., 2010a). This scheme could shift the adsorption spectrum of pure TiO_2 by creating intra-band gap states while concurrently decreasing the recombination ratio of photogenerated electron-hole pairs. Nitrogen- and nickel-co-doped TiO_2 , prepared by Zhang and Liu (2008), significantly suppressed the recombination of photo-induced electron/hole pairs due to the dispersal of Ni_2O_3 on the surface of TiO_2 . Sun et al. (2011) synthesized Pt/N- TiO_2 via a sol-gel process and showed that the prepared photocatalyst had 5.5-fold higher activity than commercially available Degussa (Evonik) P25. Such advantages have been attributed to the improved separation efficiency of photogenerated electron/hole pairs, higher interface electron transfer rate, and an increase in the number of surface hydroxyl radicals.

Most of the previous studies investigated the photocatalysis of indoor air in the near-ultraviolet or visible light regions by doped TiO_2 (Mo et al., 2009; Zhong and Haghighat, 2011). Few studies have reported the potential of using this process as a pretreatment that could be employed before biofiltration for the removal of recalcitrant VOCs.

In this study, La/N-co-doped TiO_2 photocatalysts were synthesized using a combined sol-gel and hydrothermal method. Response surface methodology (RSM) was used to produce optimum preparation conditions (molar ratios of $(\text{NH}_4)_2\text{CO}_3$, $\text{CO}(\text{NH}_2)_2$, and $\text{La}(\text{NO}_3)_3$ to Ti) during La/N- TiO_2 synthesis. The effects of La/N amount on crystal structure, particle morphology, surface element content and other structural characteristics were investigated. Chlorobenzene (CB) was used to evaluate the

photocatalytic activity of the prepared La/N-doped TiO_2 under different relative humidity (RH) values, residence times (RTs), and initial concentrations. The kinetics and mechanism of CB conversion were also studied.

1. Materials and methods

1.1. Materials

Titanium isopropoxide ($\text{Ti}(\text{O}-\text{Bu})_4$) was used as a Ti precursor. It was supplied by Aladdin Chemicals (Shanghai, China) with a purity of 97%. Urea and lanthanum nitrate ($\text{La}(\text{NO}_3)_3 \cdot 6\text{H}_2\text{O}$) were used as the N source and La source, respectively, and were supplied by Sigma-Aldrich (Shanghai, China) at 99% purity. Ammonium carbonate ($(\text{NH}_4)_2\text{CO}_3$) was used as a foaming agent and was purchased from J&K Scientific Company (Shanghai, China). Other chemicals (CB, acetylacetone, HCl, NaOH, etc.) were of analytically pure grade (Huipu Chemical Instrument Co., Ltd., Hangzhou, Zhejiang, China), and were used as received.

1.2. Preparation of photocatalyst

La/N- TiO_2 was prepared by a modified sol-gel method combined with a hydrothermal process. Ten milliliters of $\text{Ti}(\text{O}-\text{Bu})_4$, 5 mL of acetylacetone, and 50 mL absolute ethanol were mixed to prepare solution A. Then 8 mL of deionized H_2O , 20 mL absolute ethanol, 1 mL 37.5% HCl, and stoichiometric amounts of $\text{La}(\text{NO}_3)_3 \cdot 6\text{H}_2\text{O}$ (99.9%) and urea were mixed as solution B. Solution A was added dropwise into solution B at room temperature. Complete hydrolysis was reached after 2 hr of continuous mixing. After hydrolysis, the solution was aged for 6 hr and then left to evaporate at 80°C . The dried gel precursors were mixed with 60 mL NaOH (10 mol/L), 60 mL absolute ethanol, and ammonium carbonate and placed in a Teflon reactor to autoclave at 130°C for 48 hr. The prepared samples were then soaked in 37% HCl for 1 hr and separated by centrifugation. Finally, the samples were thoroughly rinsed with deionized water until the pH of the washed solution was 7.0 and air-dried at 80°C for 10 hr to obtain La/N- TiO_2 nanotubes. Un-doped TiO_2 was synthesized through the same process but without the addition of La and N precursors and was used as a reference sample alongside Degussa (Evonik) P25 (Cong et al., 2011).

The effects of La, N, and the foaming agent $(\text{NH}_4)_2\text{CO}_3$ on the photocatalytic activity of La/N- TiO_2 for CB conversion were investigated based on a three-level, three-factor Box-Behnken design (BBD, Table 1). The prepared photocatalyst was expressed as $x\text{La}/y\text{N}-\text{TiO}_2(z)$, where x, y, and z refer to the molar ratio (%) of La/Ti, N/Ti, and $(\text{NH}_4)_2\text{CO}_3/\text{Ti}$, respectively. The experimental data were analyzed with Design-Expert (V8.0.6) software for regression and graphical analyses.

1.3. Characterization of photocatalysts

UV-Visible (UV-Vis) diffuse reflectance spectra (DRS) of samples were recorded on a V650 spectrophotometer (JASCO, Japan) with BaSO_4 as a reference material. The crystalline structure of the samples was analyzed using powder X-ray diffraction (XRD) with an X'Pert PRO diffractometer (PANalytical, Holland) with $\text{Cu K}\alpha$ radiation ($\lambda = 0.154056\text{ nm}$). The micromorphology,

Table 1 – Experimental designs of the three-level along with CB conversion and predicted responses.

Run	Independent variables			CB conversion efficiency (%)	
	[La] X ₁ (%)	[N] X ₂ (%)	[(NH ₄) ₂ CO ₃] X ₃ (%)	Experimental value	Predictive value
1	0.3	0.7	1.2	83	82.57
2	0.7	0.5	0.4	82	82.39
3	0.5	0.3	0.4	80	78.78
4	0.5	0.7	0.4	83.6	84.45
5	0.5	0.7	2.0	87.2	87.6
6	0.7	0.5	2.0	84	84.84
7	0.5	0.3	2.0	83	81
8	0.3	0.5	2.0	80	80.44
9	0.3	0.5	0.4	77.2	77.19
10	0.7	0.3	1.2	81.8	81.4
11	0.7	0.7	1.2	82.9	82.08
12	0.5	0.3	1.2	81	84.3
13	0.5	0.5	1.2	93.4	93.41
14	0.5	0.5	1.2	93.8	93.41
15	0.5	0.5	1.2	93.8	93.41
16	0.5	0.5	1.2	94	93.41
17	0.5	0.5	1.2	93.7	93.41

microstructure, and particle size of the prepared photocatalyst were measured with a Tecnai G2 F30 S-Twin transmission electron microscope (TEM) equipped with energy dispersive X-ray (EDX) spectroscopy (Philips, Holland). The Brunauer–Emmett–Teller (BET) surface area and pore size distribution were evaluated by nitrogen sorption at 77 K using a Micromeritics Autosorb ASAP 2010 (Micromeritics, America). The FTIR spectra in the mid-infrared region were obtained at 4 cm^{−1} resolution on a Nicolette 6700 spectrophotometer (Thermo Electron, America) equipped with a DTGS (Deuterated Triglycine Sulfate) detector.

1.4. Photoreactor system

All experiments for the photocatalytic oxidation of CB were carried out using a quartz U-type reactor with an inner diameter of 1.4 cm and length of 50 cm. The adsorption equilibrium between reagent and photocatalyst was achieved in the dark by flowing air saturated with CB at room temperature. A 36 W mercury lamp ($\lambda = 365$ nm, Electrooptic Source Research Institute, China) was placed inside the reactor. The temperature was maintained at room temperature throughout the experiment.

Purified synthetic air with 20% O₂ and 80% N₂ was used as the carrier gas to transfer gaseous CB and water vapor into the mixing chamber where different mixing ratios were controlled by a volumetric flow meter. Gaseous CB was generated by evaporating a solution of CB at a designed initial concentration, which was determined using a mass flowmeter. The relative humidity was monitored with a hygro-thermometer (Testo 625, Testo, Germany).

1.5. Analytical methods

Quantitative analysis of CB was performed using 6980 gas chromatography with a flame ionization detector (Agilent

Technologies, America) and a carbon-hydrate analysis column (30 m × 0.32 mm × 0.25 μ m, Agilent Technologies, America). The temperature of the injector, oven, and detector was 250, 140, and 300°C, respectively. Major intermediates were determined using a 6890 N gas chromatograph coupled with a 5975 mass spectrometer detector (GC–MSD, Agilent Technologies, USA). A DB-5MS capillary column (30 m × 0.32 mm × 0.25 μ m, Agilent Technologies, USA) was used with helium as carrier gas at 1.2 mL/min. The GC oven temperature was programmed to hold at 50°C for 5 min and then increase to 280°C at 20°C/min and hold for 10 min. The MSD was run in full scan mode with $m/z = 50$ –65. The small organic acids and chloride ion content were determined with an ion chromatograph (IC) (ICS-2000, Dionex, America).

2. Results and discussion

2.1. RSM model analysis for preparation of the photocatalyst

The optimum conditions for the preparation of photocatalysts were determined using experimental designs across three levels with experimental values, and the responses of CB conversion were predicted at 365 nm (Table 1). A semiempirical second-order polynomial expression in Eq. (1) consisted of 10 statistically significant coefficients, which were obtained from the analysis of variance (ANOVA) at 95% confidence level ($p < 0.05$).

$$R = -36.46 + 245.34[(\text{NH}_4)_2\text{CO}_3] + 200.02[\text{N}] + 17.87[\text{La}] - 66.25[(\text{NH}_4)_2\text{CO}_3][\text{N}] - 1.25[(\text{NH}_4)_2\text{CO}_3]^2 + 0.94[\text{N}][\text{La}] - 198.72[(\text{NH}_4)_2\text{CO}_3]^2 - 153.09[\text{N}]^2 - 6.64[\text{La}]^2 \quad (1)$$

where, R (%) is the CB conversion efficiency.

This model was a good fit throughout the experimental range ($R^2 = 0.9653$), as indicated by the experimental values and predicted responses (Fig. S1). The inset in Fig. 1 shows that the residual plots for models and dataset had a random distribution, which indicated that the residual distribution was suitable for representing the relationship between conversion efficiency and the above parameters. High significance was observed, as indicated by a large F -value and a small p -value ($p < 0.05$; Table S1).

The $[(\text{NH}_4)_2\text{CO}_3]$, $[\text{N}]$, and $[\text{La}]$ variables were all found to be highly significant; their p -values were as low as 0.05. This response indicates that CB conversion efficiency was significantly affected by $[(\text{NH}_4)_2\text{CO}_3]$, $[\text{N}]$, and $[\text{La}]$. The p -value of the interaction variable $[(\text{NH}_4)_2\text{CO}_3][\text{N}]$ was 0.0492, indicating that this interaction was also highly significant. The + and − signs of the coefficients here represent positive and negative effects, respectively. $[(\text{NH}_4)_2\text{CO}_3]$, $[\text{N}]$, $[\text{La}]$, and $[\text{N}][\text{La}]$ showed positive influences on CB conversion, and $[(\text{NH}_4)_2\text{CO}_3][\text{N}]$, $[(\text{NH}_4)_2\text{CO}_3]^2$, $[\text{N}]^2$, and $[\text{La}]^2$ had negative influences (Vildozo et al., 2010).

The two-dimensional contour and three-dimensional response surface plots were used to determine the confidence of response factors for CB conversion. The response surface with $[\text{La}]$ was 1.2 (Fig. S2). ANOVA analysis showed that $[(\text{NH}_4)_2\text{CO}_3][\text{N}]$ had a significant influence on the conversion of CB. There was a partial maximum region under the variables range of $[(\text{NH}_4)_2\text{CO}_3]$ and $[\text{N}]$. The conversion efficiency

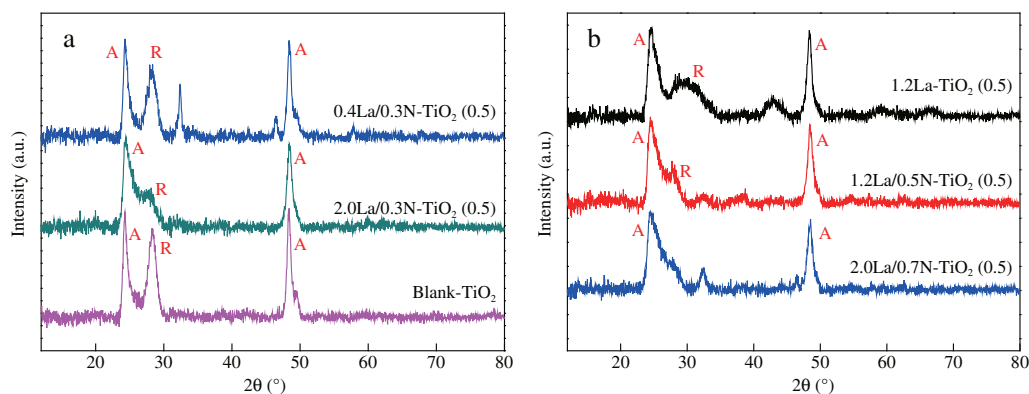


Fig. 1 – XRD spectra of the synthesized photocatalysts. A represents Anatase TiO_2 ; R represents Rutile TiO_2 . XRD: X-ray diffraction.

improved when the $[(\text{NH}_4)_2\text{CO}_3]$ value increased within the optimal level regardless of whether the [N] value was high or low. However, the conversion efficiency decreased as $[(\text{NH}_4)_2\text{CO}_3]$ increased, even beyond the optimal level, when the [N] values changed. The range of CB conversion efficiency was more obvious at low levels of [N] than at high levels. The CB conversion efficiency increased with $[(\text{NH}_4)_2\text{CO}_3]$ and [N] values from 0.3 to 0.5. Values above 0.5 decreased conversion efficiency. From the response surface analysis, the optimal conditions of $[(\text{NH}_4)_2\text{CO}_3]$, [N], and [La] were 0.52, 0.54, and 1.33, respectively. With this in mind, the optimum photocatalyst prepared was 1.2La/0.5 N-Ti(0.5).

2.2. Characterization of photocatalysts

2.2.1. XRD results

The XRD patterns of the photocatalysts are reported in Fig. 1. Anatase and rutile crystal phases were the two main polymorphs present in all samples, but they were present at different ratios. The introduction of La into the crystal structure of TiO_2 was found to affect the phase transformation from anatase to rutile (Kiatkittipong et al., 2011; Kim et al., 2012). When the percentage of La increased from 0% to 2%, the rutile peak (110) at 2θ of 27.3° became broader and weaker. When the La percentage increased beyond 2%, the rutile peak for this value of 2θ could not be identified. According to the Spurr-Myers formula, the ratios of anatase vs. rutile were 0.298, 0.316, and 0.645 for 0.4La- TiO_2 , 1.2La- TiO_2 , and 2.0La- TiO_2 , respectively. This indicates that La-doping could promote or hinder the growth of different crystal structures (Li et al., 2004; Van der Meulen et al., 2007). Higher ratios of anatase to rutile may facilitate higher photocatalytic activity. This is similar to the highly active mixed phase titania P25. In Fig. 1a for the sample of 0.4La/0.3N- TiO_2 (0.5), there was also a peak at about 2θ of 32° , which might belong to La-oxide (2θ in the JCPDS standard card is about 30.7°). Its appearance could be attributed to an uneven dispersion of La-oxide on the surface of TiO_2 with some La entering into the lattice (Gao et al., 2008). The peak at 2θ of 25.4° would be the characteristic one for nanotubes, as reported by several studies, and also was present in the prepared catalysts, indicating that the nanotubes might have the rutile phase. Further study on the nanotubes' crystal phase will be carried by Raman spectroscopy.

N was found to be incorporated into TiO_2 , but did not alter the crystal structure of La- TiO_2 much more (Fig. 1b). N only broadened the rutile peak or even made this peak disappear (2θ of 43.7° appeared in the sample of 1.2La- TiO_2 (0.5) but not in other samples). Gurkan et al. (2012) reported that the XRD patterns of N- TiO_2 were similar to those of P25 TiO_2 . These findings suggested that N atoms could be incorporated into the TiO_2 structure interstitially, substitutionally, or both ways, which may affect other properties, such as the optical properties of TiO_2 (see Section 2.2.4).

The average sizes of the crystals formed by the different prepared photocatalysts were estimated based on Scherrer's equation using the full-width at half maximum of the anatase (101 and 200) and rutile (110) peaks. The sizes of the crystals produced using other synthesized nanotubes (0.4La/0.3N- TiO_2 (0.5) and 1.2La/0.3N- TiO_2 (0.5)) were comparable to that of the optimum 1.2La/0.5N- TiO_2 (0.5), 6 nm. The reference nanotubes were 8 nm in size. The addition of N was found to reduce crystal size, and this may influence the hydrolysis and condensation rates of the metal alkoxide, thus restricting TiO_2 growth during synthesis (Chen et al., 2012; Gurkan et al., 2012). These lower crystallite sizes are reflected in the BET surface areas of nano-sized samples, which were much higher than the reference values for TiO_2 (Table 3).

2.2.2. TEM and EDX analysis

TEM was used to further characterize the morphological features exhibited by the co-doped TiO_2 nanotubes. Selected micrographs of prepared samples, including reference TiO_2 nanotubes and 1.2La/0.5N- TiO_2 (0.5), are shown in Fig. 2. The micrograph of 1.2La/0.5N- TiO_2 (0.5) also presents EDX data, with a corresponding table of the detected atomic ratios. Fig. 2a and b show that both samples had nanotubes that were randomly oriented. The 1.2La/0.5N- TiO_2 (0.5) sample had a less dense structure, a more uniform shape, and less agglomeration than the reference. The incorporation of the foaming agent $(\text{NH}_4)_2\text{CO}_3$ may affect the packing of the nanotubes forming during synthesis. When TiO_2 precursors and $(\text{NH}_4)_2\text{CO}_3$ were treated together at 130°C in a Teflon reactor, the latter was completely decomposed into CO_2 , H_2O and NH_3 with generation of gas bubbles. Energy was released when these bubbles exploded. This energy generated an effect similar to the cavitation effect of ultrasound (Chen et al.,

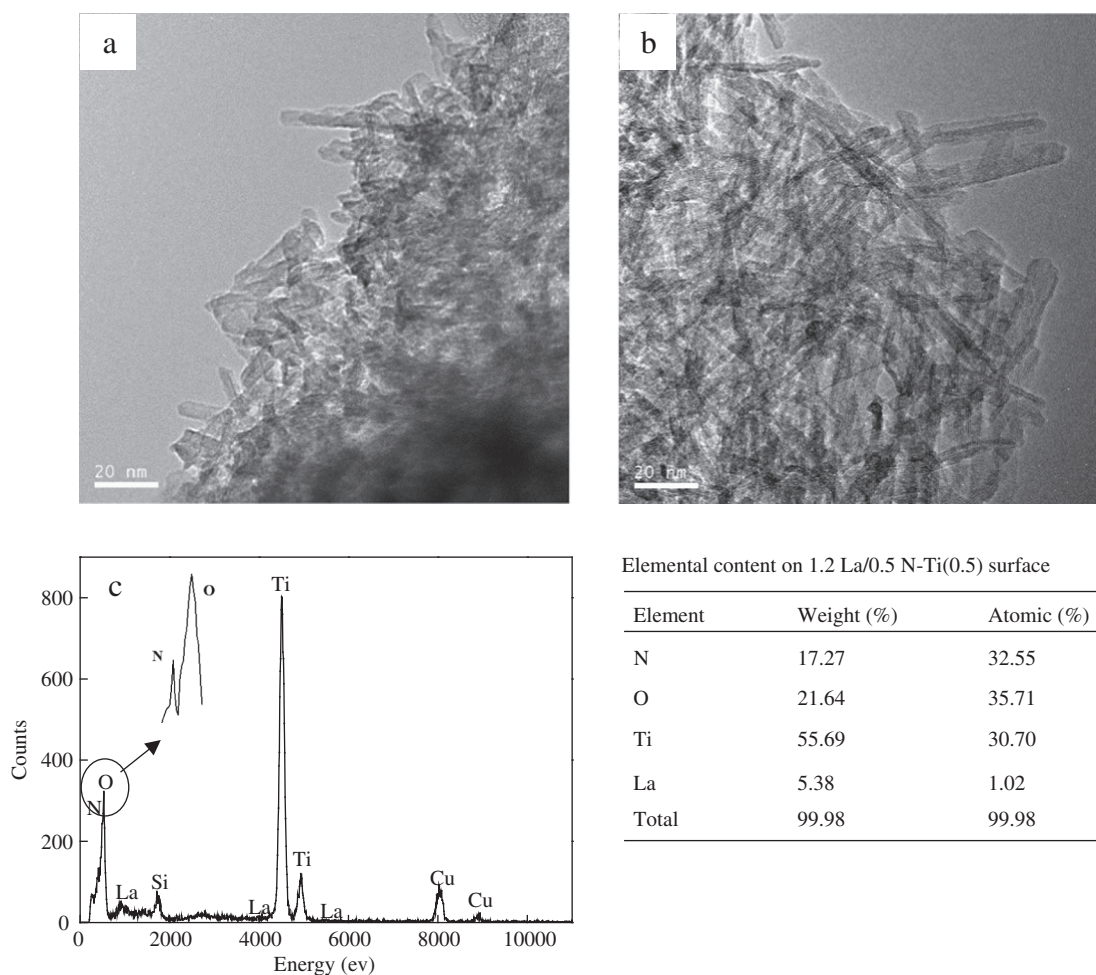


Fig. 2 – TEM images of blank TiO_2 (a) and $1.2\text{La}/0.5\text{N-TiO}_2(0.5)$ (b) with EDX spectroscopy (c) and elemental analysis (inset Table). TEM: Transmission Electron Microscopy; EDX: Energy Dispersive X-ray.

2012). Such energy being released in a short time prevents the agglomeration of synthesized TiO_2 (Ding and Pacek, 2008). Kapusuz et al. (2013) obtained better dispersion and less aggregation for B–Zr co-doped TiO_2 , which was found to have a higher photocatalytic activity than a sample with higher aggregation under UV-irradiation. The average diameters of the synthesized nanotubes were 8 and 6 nm for reference TiO_2 and $1.2\text{La}/0.5\text{N-TiO}_2(0.5)$, respectively. This demonstrated that La and N co-doping could inhibit further increases in nanotube diameter.

As shown in Fig. 2c and the inset table, both La and N were present in the structure of TiO_2 . There were no bonds assignable to Ti and La or Ti and N, which indicated that N and La atoms were interstitially embedded in the TiO_2 lattice. It might be speculated that such atoms successfully incorporated into TiO_2 and allowed the prepared photocatalyst to be activated under longer wavelength irradiation (Joshi et al., 2009; Zhang et al., 2013).

2.2.3. BET results

Table 2 shows the value of BET surface area using both reference and commercial TiO_2 and the prepared photocatalysts. The optimum photocatalysts had a larger surface area and total

volume than P25 (about 7-fold), even though the prepared samples and commercial P25 both were nano-sized. The same synthesis methodology made the reference TiO_2 also have high surface area without any element addition. The addition of La, N, and ammonium carbonate slightly increased the total surface area and decreased the pore size (Cheng et al., 2013; Wei et al., 2013). Among all the samples synthesized, $1.2\text{La}/0.5\text{N-TiO}_2(0.5)$ had the largest surface area and smaller pore size than the other two samples, which also confirms the accuracy of the prediction of the RSM model analysis. In addition, the average pore sizes of

Table 2 – Properties of P25 and as-prepared TiO_2 composites.

Photocatalysts	S_{BET} (m^2/g)	BJH Total volume ($\times 10^{-2} \text{ cm}^3/\text{g}$)	BJH average pore size (nm)
P25	55.7	11.6	7.3
Blank TiO_2	335.0	73.8	8.05
$1.2\text{La}/0.5\text{N-Ti}(0)$	375.6	66.8	6.21
$1.2\text{La}/0.5\text{N-Ti}(0.5)$	395.5	67.9	6.38
$2.0\text{La}/0.5\text{N-Ti}(0.3)$	380.1	67.2	6.06
$2.0\text{La}/0.5\text{N-Ti}(0.7)$	375.7	65.6	6.07

reference TiO_2 and $1.2\text{La}/0.5\text{N-TiO}_2(0.5)$ were 8 and 6 nm, respectively, which are in agreement with the TEM data.

The adsorption between a pollutant and photocatalyst can be increased by increasing surface area and decreasing pore size (Li et al., 2011; Yu et al., 2012) and the subsequent photocatalytic reaction could then happen more efficiently.

2.2.4. UV-Vis spectroscopy

The optical properties of the prepared samples were studied by UV-Vis spectroscopy, and the diffuse reflection spectra are shown in Fig. 3. It was found that the absorption edge was extended into longer wavelengths with N or/and La doping. The band gap of all photocatalysts was calculated with the Kubelka-Munk transition equation by extrapolating the absorption edge onto the energy axis. The calculated gap energies of the reference TiO_2 and $1.2\text{La}/0.5\text{N-TiO}_2(0.5)$ were 3.11 and 2.95 eV. Other values obtained for $1.2\text{La}/0.5\text{N-TiO}_2(0.5)$, $0.5\text{N-TiO}_2(0.5)$, and $1.2\text{La}/0.7\text{N-TiO}_2(0.7)$ were 3.08, 2.98, and 2.92 eV, respectively.

La/N-co-doped TiO_2 exhibited absorption in the visible light region near 400 nm, and the reference TiO_2 spectrum did not show any red shift. The incorporation of different elements leads to a red shift, and in the present study the role of N could be much larger than that of La. The reason might be that the mixture of N 2p and O 2p orbit electron states formed could narrow the band gap of TiO_2 and consequently extend the photo-response into longer wavelengths (Sun et al., 2013). It was also found La/N co-doping could further promote the occurrence of a red shift, and the absorption edge changed slightly as the N:Ti molar ratio changed from 0.5 to 0.7. It has been reported that the formation of localized intra-gap states above the upper level of the valence band by nitrogen doping is responsible for the new absorption band (Soares et al., 2011). The results of other studies were consistent with those showing lower band gap energy values and broadened photoabsorption regions (Bacsa et al., 2005; Chen et al., 2007; Dolat et al., 2012).

2.2.5. FTIR spectra

Fig. 4 compares the FTIR spectra of reference TiO_2 and $1.2\text{La}/0.5\text{N-TiO}_2(0.5)$ photocatalysts. For the $1.2\text{La}/0.5\text{N-TiO}_2(0.5)$ sample, there were two absorption peaks near 585 and 1060 cm^{-1} that were not present in reference TiO_2 . These peaks were assigned to Ti-O-La and N-Ti-O bands, respectively (Yang et al., 2011; Kapusuz et al., 2013). These new bonds indicated that the La and N were successfully doped interstitially into TiO_2 . This result is consistent with the EDX and UV-Vis analysis given above, which showed that the defects in the lattice on the TiO_2 surface facilitated La and N doping, which was responsible for the visible light absorption.

The absorption peaks at 1630 and 3400 cm^{-1} were attributed to the bending vibration of surface hydroxyl and the stretching vibration of hydroxyl within the structure. These were formed by hydrogen bonds on the surface of water molecules and by group bonding to titanium atoms, respectively (Huang et al., 2009). The intensity of the two peaks attributed to the free OH bond and the Ti-OH-Ti bond increased in the La-N co-doped photocatalyst, indicating that there were more surface-adsorbed hydroxyl groups after La-N co-doping. The hydroxyl groups are hydrophilic and play

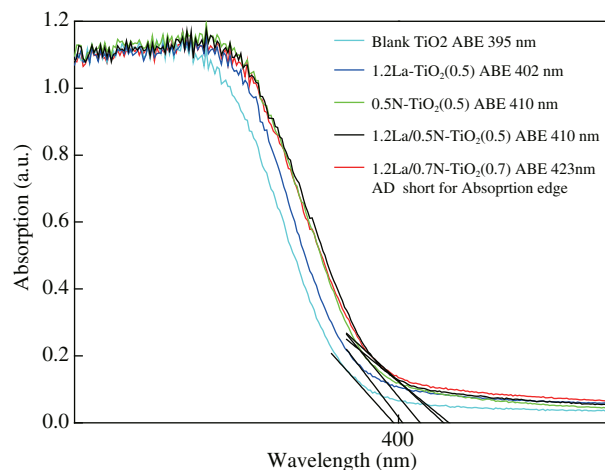


Fig. 3 – UV-Vis diffuse reflection absorption spectrum of as-prepared photocatalysts.

an important role in the photocatalytic process of TiO_2 . The degree of adsorption of pollutants like CB is a function of the hydrophilicity of the photocatalyst. Furthermore, the surface hydroxyl groups could also react with holes to generate active oxygen species and thus prolong the separation of current carriers. For these reasons, La-N co-doped TiO_2 is expected to be more efficient than undoped photocatalysts in the conversion of VOCs.

2.3. Photocatalytic conversion of CB

N-La co-doping could enhance the prepared catalyst's characteristics such as response to a longer wavelength (365 nm), larger surface area (easily adsorbing much more reactants), and the formation of Ti-OH-Ti species (inhibiting the competition between water and the target species). All these characteristics would be better for the conversion of volatile organic compounds (CB, etc.), especially in relatively high RH. The photocatalytic conversion of CB was investigated, using

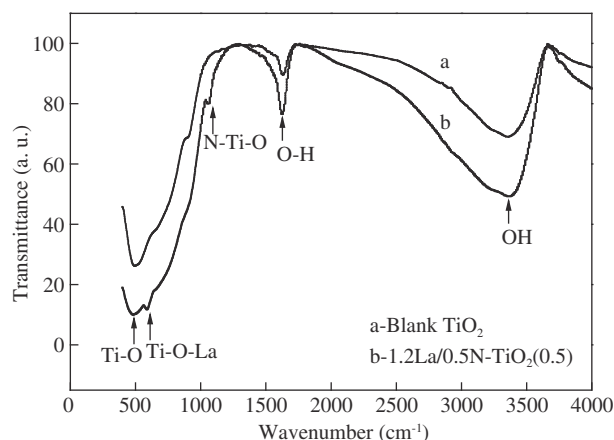


Fig. 4 – Fourier Transform Infrared Spectroscopy (FT-IR) spectra of blank TiO_2 and $1.2\text{La}/0.5\text{N-TiO}_2(0.5)$ photocatalysts.

the optimal prepared catalyst 1.2La/0.5N-TiO₂(0.5) irradiated with 365 nm UV light. The photo-oxidation of CB proceeded only in the presence of both catalyst and UV irradiation. The influence of relative humidity (RH), initial concentration of CB and reaction time (RT) on the photocatalytic efficiency of co-doped TiO₂ nanotubes was studied.

The different findings presented below can be explained by considering the adsorption capacity of different chemical compounds and of the different surface characteristics of the catalysts (Dong et al., 2008; Tomašić et al., 2008; Debono et al., 2011). Fig. 5 shows the effects of RH on the conversion of CB. RH values between 10% and 70% did not influence the conversion of CB, but values over 80% inhibited its conversion. Generally, catalytic reaction of hydrophobic VOCs is inhibited under humid conditions (RH over 30%) because of competition adsorption between water and hydrophobic VOCs (Guo et al., 2008). Such competition would increase the concentration of Ti–OH–Ti species (characterized by the 3000–3450 cm^{−1} FTIR band). The lower the intensity of this band, the greater the water adsorption by these active sites on the surfaces of catalysts. For 1.2La/0.5N-TiO₂(0.5), the concentration of Ti–OH–Ti species was higher, indicating that the competition between water and CB were relatively low. Therefore, the conversion of CB would not be inhibited at RH 60%–70%. At RH values over 80%, more water molecules hinder the effective absorption of light for the catalyst, impeding the oxidation reaction.

Some hydrophilic VOCs can penetrate the water monolayers and become adsorbed on the catalyst surface more effectively than others. In this case, RH had a positive effect on the conversion of CB, but excessively high RH values can also lower the conversion rate because of the limited amount of light that reaches the catalyst's surface (Geng et al., 2010). This is consistent with the results observed for RH over 80%, which indicated that the prepared catalyst should have broad applications in the treatment of industrial waste gas at RH values of 50%–70%.

The effects of initial CB concentration and RT on the photocatalytic conversion of CB at RH of 10% are shown in Fig. 5b. The photolysis line indicates the conversion of 100 mg/m³ CB below 365 nm without any catalysts. At higher concentrations, the conversion rate was lower, although very

fast initial kinetics were observed. After that, conversion slowed down, which is a typical behavior in heterogeneous photocatalysis. The parent compound, in this case CB, was rapidly transformed into other oxidation products, causing competition for the active sites, forming radicals and lowering the photocatalytic activity (Akly et al., 2010; Sakai et al., 2003).

2.4. Kinetics analysis

The Langmuir–Hinshelwood (L–H) kinetic model was used to calculate the heterogeneous photocatalytic reaction rates of CB degradation. This model was used for the data obtained from several VOC photocatalytic conversions: (Joshi et al., 2009; Cheng et al., 2013)

$$r = \frac{k_r KC}{1 + KC} \quad (2)$$

where, r is the photocatalytic conversion rate, k_r (mg/(m³·min)) is the reaction rate constant, K (m³/mg) is the adsorption rate constant, and C is the initial concentration of CB. Here, the products k_r and K were defined as the apparent first-order rate constant k_{app} . The R^2 coefficients of 0.9992, 0.9928, and 0.9875, respectively, indicated that CB conversion fit the L–H model well at low humidity (Fig. 6). This might be because the L–H model was more suitable for photocatalytic conversion in the absence of water vapor.

However, in the presence of water vapor, there was a competitive adsorption effect between the water vapor and the CB. For this reason, five models were used based on different assumptions (Table 3). RSS (Residual sum of squares) and MRSS (Mean residual sum of squares) are the residual sum of squares and the mean residual sum of squares, respectively. These were calculated using the Marquardt–Levenberg method according to Korologos et al. (2011).

As shown in Table 3, the third and the fifth models (M–L–H3 and M–L–H5) were far superior to the others in describing the experimental data obtained in the presence of water. The first model was insufficient to describe all the experimental results because it assumed that water did not take part in the CB conversion. The models demonstrated that water vapor played a key role in the photocatalysis of CB.

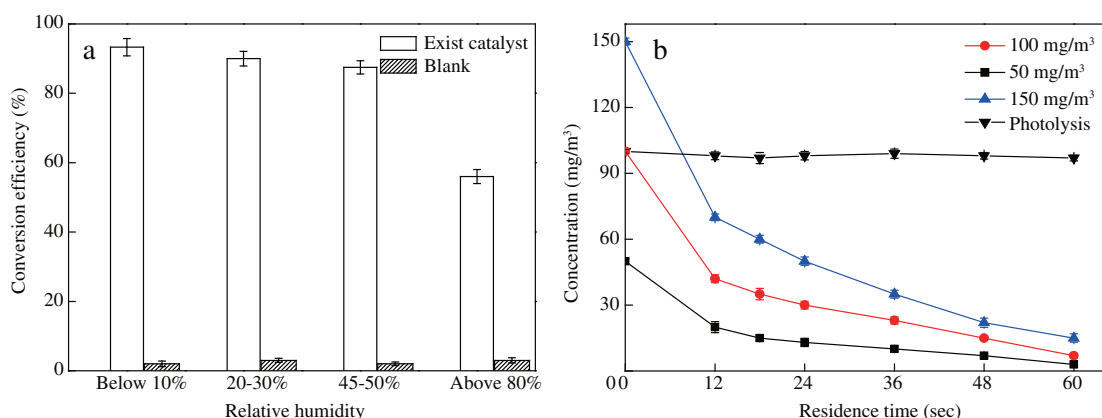


Fig. 5 – Effects of RH on the conversion of CB (a) and relationship between residence time and initial concentration on the outlet concentration of CB (b). RH: relative humidity.

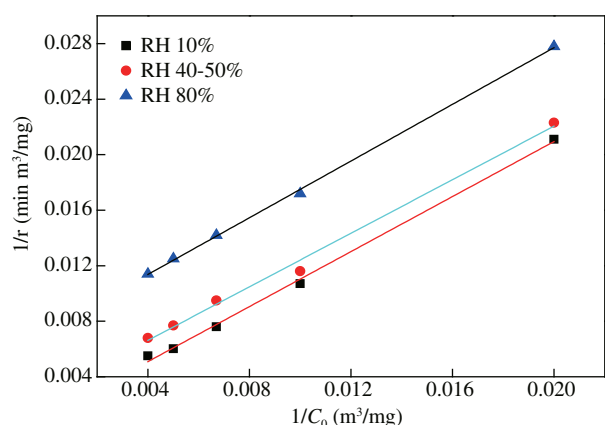


Fig. 6 – Langmuir–Hinshelwood model for the 1-CB photoconversion under different RHs. The reaction time was 60 s, and the initial concentration of 1-CB ranged 50 to 150 mg/m³. RH: relative humidity.

The addition of water to the feed led to a significant increase in the rate constant (3-fold) especially at RH 10% and 40%–50%. The increases in the rate constants at different RH values were attributed to different amounts of adsorption of CB or water vapor. When the RH was over 80%, however, the CB rate constant decreased. This was attributed to the large amount of water vapor occupying the active sites on the surface of the photocatalyst, which in turn influenced the CB adsorption. This was consistent with the results shown in both Fig. 6 and previous studies (Larson and Falconer, 1997;

Sakai et al., 2003; Joshi et al., 2009; Korologos et al., 2011; Zhang et al., 2013).

The values of RSS and MRSS indicated that these values from the same model increased with humidity, indicating that the models had limitations with respect to describing the conversion of CB at higher values of RH. This might be because the models neglected the competitive adsorption of the by-products (Vincent et al., 2009; Mo et al., 2013). Adsorption of by-products could be neglected at low water vapor levels, but it also might influence the conversion of reactants under humid conditions. For this reason, the models in Table 3 were not appropriate for description of conversion at higher RH values or at higher concentrations of CB.

2.5. Possible reaction pathway of CB with La/N–TiO₂

The intermediate products in the photocatalytic oxidation of 100 mg/m³ CB using La–N co-doped TiO₂ catalyst under 365 nm light were analyzed by GC–MS and IC. Table S2 lists all the intermediates and the methods by which they were detected and their characteristics. Here, 3-chlorophenol and *p*-chlorophenol were detected but *o*-chlorophenol was not. This suggests that the active radicals on the surface of catalyst attacked the para- and meta-positions on benzene ring first (Vincent et al., 2009). Other intermediates detected included ethylene glycol, lactic acid, glycerol, *m*-dihydroxybenzene, salicylic acid, 4-hydroxybenzoic acid, dodecanoic acid, 1-butanol, formic acid, acetic acid, and oxalic acid.

The conversion of CB was attributed to the generation of $\cdot\text{OH}$ and O_2^- as main oxidants and to the highly active ring generated after photoactivation during photocatalysis under the conditions tested (Zhang et al., 2007; Han et al., 2013). A proposed photocatalytic oxidation pathway of CB by La–N co-doped TiO₂ catalyst under 365 nm light irradiation was proposed based on the intermediates identified after different accumulation periods (Fig. 7).

First, $\cdot\text{OH}$ and O_2^- directly attacked the hydrogen atom on the benzene ring and the hydroxide radical replaced the hydrogen atom to generate chlorophenol compounds (D1). This was found to be the main process of photocatalytic degradation of CB in a previous report (Zhang et al., 2007). The chlorophenol compounds continued to be attacked by $\cdot\text{OH}$ to form *p*-dihydroxybenzene, *m*-dihydroxybenzene, and *o*-dihydroxybenzene (D2). The rings of these compounds were easily opened and a series of small molecules formed, specifically aliphatic alcohols and smaller molecules (D3 and D4). Second, D1 was converted to salicylic acid and 4-hydroxybenzoic acid (D5) via the replacement of chloride ions by $\cdot\text{OH}$ and $\cdot\text{OOH}$. Third, $\cdot\text{OH}$ directly attacked the hydrogen atom on the benzene ring, forming an opening in the phenol ring and further oxidizing its target to aliphatic alcohols (D6) and some small acid intermediates. The main intermediates were 4-hydroxybenzoic, 3-chlorophenol, and *p*-chlorophenol. These results demonstrated that the main degradation pathway for the photocatalytic oxidation of CB was $\text{CB} \rightarrow 3\text{-chlorophenol}/p\text{-chlorophenol} \rightarrow 4\text{-hydroxybenzoic acid} \rightarrow \text{short chain alcohol/acid} \rightarrow \text{CO}_2 + \text{H}_2\text{O}$.

Interestingly, all of the by-products observed in this study were successfully converted to soluble or low-toxicity

Table 3 – Rate and adsorption constants for CB and model in the presence.

RH	Model ^a	K_{app}	K	K_W	RSS	MRSS
<1	L-H	1.01	0.00184	–	–	–
	L-H	1.04	0.00136	–	–	–
	M-L-H1	1.81	0.00018	10^{-6}	4.28	0.29
	M-L-H2	2.31	0.00098	0.00087	5.60	0.37
	M-L-H3	3.00	0.00097	0.00049	0.27	0.01
40%–50%	M-L-H4	2.24	0.00023	0.00064	0.98	0.08
	M-L-H5	2.89	0.00047	0.00071	2.38	0.17
	L-H	1.00	0.00231	–	–	–
	M-L-H1	2.01	0.00198	0.00012	24.23	0.74
	M-L-H2	2.98	0.00174	0.00178	12.14	0.39
	M-L-H3	3.07	0.00204	0.00168	0.78	0.06
	M-L-H4	2.54	0.00187	0.00187	13.45	0.42
	M-L-H5	3.07	0.00211	0.00195	0.68	0.37
	L-H	0.93	0.00541	–	–	–
	M-L-H1	0.98	0.00038	10^{-6}	123.1	4.18
>80%	M-L-H2	1.05	–	0.00214	28.46	0.76
	M-L-H3	2.68	0.00189	0.00246	15.23	0.41
	M-L-H4	2.47	0.00198	0.00278	13.24	0.36
	M-L-H5	2.85	0.00321	0.00301	8.21	0.24

^a M-L-H1: $R_a = k_R \times (K_A C_A) / (1 + K_A C_A + K_W C_W)$.
M-L-H2: $R_a = k_R \times (K_A C_A K_W C_W) / (1 + K_A C_A + K_W C_W)^2$.
M-L-H3: $R_a = k_R \times (K_A C_A K_W C_W) / (1 + K_A C_A)(1 + K_W C_W)$.
M-L-H4: $R_a = k_R \times (C_A K_W C_W) / (1 + K_W C_W)$.
M-L-H5: $R_a = k_R \times (K_A C_A K_W C_W)^{0.5} / (1 + (K_W C_W)^{0.5} + (K_W C_W)^{0.5})^2$.

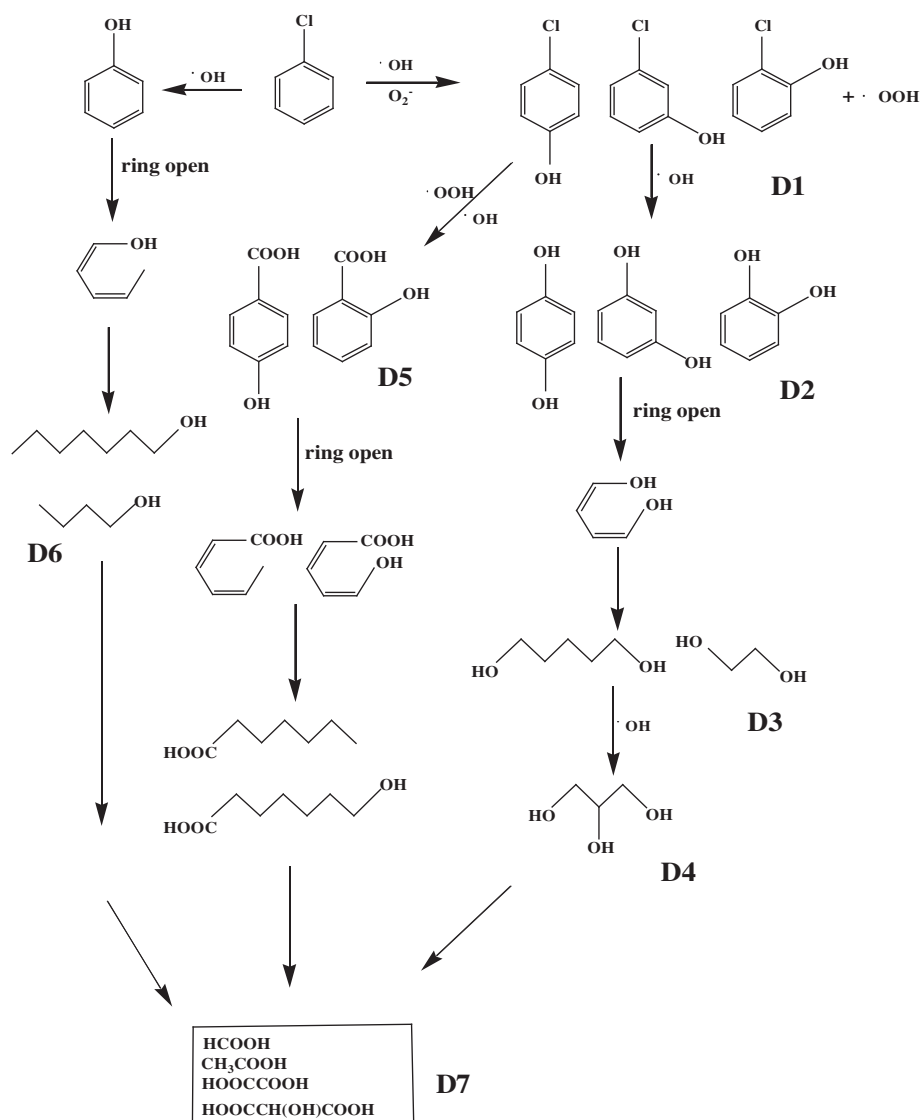


Fig. 7 – Possible conversion pathway for photocatalytic oxidation of CB. CB: chlorobenzene.

chemicals containing $-\text{OH}$, $-\text{O}$, or $-\text{H}$ bonds (Table S2). Consequently, the photocatalytic process did not completely convert CB into mineralized compounds. The rest of the hydrophilic by-products can still be removed easily through a biological process such as bio-trickling filtration.

3. Conclusions

La/N-TiO₂ nanotubes were efficiently prepared by a novel sol-gel/hydrothermal method. The optimum photocatalyst obtained was 1.2La/0.5N-TiO₂(0.5) as determined by RSM model analysis. A thorough characterization indicated the presence of N and La as O-Ti-N and O-Ti-La species as well as a surface area of 380.1 m²/g, with calculated gap energy of 2.95 eV. The addition of ammonium carbonate also contributed to enhanced structural and morphological properties for the synthesized nanotubes. The photocatalytic activity was successfully tested, with high conversion rates for CB under 365 nm light. The

relative humidity of the system was found to have a positive effect on the conversion of CB at values below 70%, but inhibition was observed at values higher than 80% RH. This provides new insight into the effect of water molecules on the photocatalytic efficiency of doped TiO₂. Kinetic analysis showed that the L-H model was a good fit for the experimental data because it includes the reaction between VOC and water adsorbed on different active sites. These results demonstrate that the La/N-TiO₂ has considerable potential for the conversion of environmentally hazardous gaseous compounds under longer UV wavelengths.

Acknowledgments

This work was supported by the National Natural Science Foundation of China (No. 21276239), the Program for Changjiang Scholars and Innovative Research Team in University (No. IRT13096). We would like to thank LetPub

(www.letpub.com) for its linguistic assistance during the preparation of this manuscript and the anonymous reviewers for their constructive criticism of the manuscript.

Appendix A. Supplementary data

Supplementary data to this article can be found online at <http://dx.doi.org/10.1016/j.jes.2015.09.026>.

REFERENCES

- Adjimi, S., Roux, J.C., Sergent, N., Delpech, F., Thivel, P.X., Pera-Titus, M., et al., 2014. Photocatalytic oxidation of ethanol using paper-based nano-TiO₂ immobilized on porous silica: A modelling study. *Chem. Eng. J.* 251, 381–391.
- Akly, C., Chadik, P.A., Mazyck, D.W., 2010. Photocatalysis of gas-phase toluene using silica-titania composites: Performance of a novel catalyst immobilization technique suitable for large-scale applications. *Appl. Catal. B Environ.* 99 (1–2), 329–335.
- Bacsa, R.R., Kiwi, J., Ohno, T., Albers, P.W., Nadtochenko, V.A., 2005. Preparation, testing and characterization of doped TiO₂ active in the peroxidation of biomolecules under visible light. *J. Phys. Chem. B* 109 (12), 5994–6003.
- Chen, D.M., Jiang, Z.Y., Geng, J.Q., Wang, Q., Yang, D., 2007. Carbon and nitrogen co-doped TiO₂ with enhanced visible-light photocatalytic activity. *Ind. Eng. Chem. Res.* 46 (9), 2741–2746.
- Chen, J.Y., Wang, H.J., Wei, X.Z., Zhu, L.P., 2012. Characterization, properties and catalytic application of TiO₂ nanotubes prepared by ultrasonic-assisted sol-hydrothermal method. *Mater. Res. Bull.* 47 (11), 3747–3752.
- Cheng, Z.W., Feng, L., Chen, J.M., Yu, J.M., Jiang, Y.F., 2013. Photocatalytic conversion of gaseous ethylbenzene on lanthanum-doped titanium dioxide nanotubes. *J. Hazard. Mater.* 254–255, 354–363.
- Cong, Y., Tian, B.Z., Zhang, J.L., 2011. Improving the thermal stability and photocatalytic activity of nanosized titanium dioxide via La³⁺ and N co-doping. *Appl. Catal. B Environ.* 101 (3–4), 376–381.
- Debono, O., Thevenet, F., Gravejat, P., Hequet, V., Raillard, C., Lecoq, L., et al., 2011. Toluene photocatalytic oxidation at ppbv levels: Kinetic investigation and carbon balance determination. *Appl. Catal. B Environ.* 106 (3–4), 600–608.
- Ding, P., Pacek, A.W., 2008. De-agglomeration of goethite nano-particles using ultrasonic comminution device. *Powder Technol.* 187 (1), 1–10.
- Dolat, D., Quici, N., Kusiak-Nejman, E., Morawski, A.W., Puma, G.L., 2012. One-step, hydrothermal synthesis of nitrogen, carbon co-doped titanium dioxide (N, C-TiO₂) photocatalysts. Effect of alcohol degree and chain length as carbon dopant precursors on photocatalytic activity and catalyst deactivation. *Appl. Catal. B Environ.* 115, 81–89.
- Dong, F., Zhao, W.R., Wu, Z.B., 2008. Characterization and photocatalytic activities of C, N and S co-doped TiO₂ with 1D nanostructure prepared by the nano-confinement effect. *Nanotechnology* 19 (36), 365607.
- Gao, J., Hou, Z.Y., Guo, J.Z., Zhu, Y.Z., Zheng, X.M., 2008. Catalytic conversion of methane and CO₂ to synthesis gas over a La₂O₃-modified SiO₂ supported Ni catalyst in fluidized-bed reactor. *Catal. Today* 131 (1–4), 278–284.
- Geng, Q.J., Guo, Q.J., Yue, X.H., 2010. Adsorption and photocatalytic degradation kinetics of gaseous cyclohexane in an annular fluidized bed photocatalytic reactor. *Ind. Eng. Chem. Res.* 49 (10), 4644–4652.
- Guo, T., Bai, Z.P., Wu, C., Zhu, T., 2008. Influence of relative humidity on the photocatalytic oxidation (PCO) of toluene by TiO₂ loaded on activated carbon fibers: PCO rate and intermediates accumulation. *Appl. Catal. B Environ.* 79 (2), 171–178.
- Gurkan, Y.Y., Turkten, N., Hatipoglu, A., Cinar, Z., 2012. Photocatalytic degradation of cefazolin over N-doped TiO₂ under UV and sunlight irradiation: Prediction of the reaction paths via conceptual DFT. *Chem. Eng. J.* 184, 113–124.
- Han, Z.N., Chang, V.W., Wang, X.P., Lim, T.T., Hildemann, L., 2013. Experimental study on visible-light induced photocatalytic oxidation of gaseous formaldehyde by polyester fiber supported photocatalysts. *Chem. Eng. J.* 218, 9–18.
- Huang, D.G., Liao, S.J., Zhou, W.B., Quan, S.Q., Liu, L., He, Z.J., et al., 2009. Synthesis of samarium- and nitrogen-co-doped TiO₂ by modified hydrothermal method and its photocatalytic performance for the degradation of 4-chlorophenol. *J. Phys. Chem. Solids* 70 (5), 853–859.
- Joshi, M.M., Labhsetwar, N.K., Mangrulkar, P.A., Tijare, S.N., Kamble, S.P., Rayalu, S.S., 2009. Visible light induced photoreduction of methyl orange by N-doped mesoporous titania. *Appl. Catal. A Gen.* 357 (1), 26–33.
- Kapusuz, D., Park, J., Ozturk, A., 2013. Sol-gel synthesis and photocatalytic activity of B and Zr co-doped TiO₂. *J. Phys. Chem. Solids* 74 (7), 1026–1031.
- Kennes, C., Veiga, M.C., 2010. Technologies for the abatement of odours and volatile organic and inorganic compounds. *Chem. Eng. Trans.* 23, 1–6.
- Kiatkittipong, K., Scott, J., Amal, R., 2011. Hydrothermally synthesized titanate nanostructures: impact of heat treatment on particle characteristics and photocatalytic properties. *ACS Appl. Mater. Interfaces* 3 (10), 3988–3996.
- Kim, G., Choi, W., 2010. Charge-transfer surface complex of EDTA-TiO₂ and its effect on photocatalysis under visible light. *Appl. Catal. B Environ.* 100 (1–2), 77–83.
- Kim, S., Kim, M., Hwang, S.H., Lim, S.K., 2012. Enhancement of photocatalytic activity of titania-titanate nanotubes by surface modification. *Appl. Catal. B Environ.* 123, 391–397.
- Korologos, C.A., Philippopoulos, C.J., Pouloupoulos, S.G., 2011. The effect of water presence on the photocatalytic oxidation of benzene, toluene, ethylbenzene and m-xylene in the gas-phase. *Atmos. Environ.* 45 (39), 7089–7095.
- Larson, S.A., Falconer, J.L., 1997. Initial reaction steps in photocatalytic oxidation of aromatics. *Catal. Lett.* 44 (1–2), 57–65.
- Leethochawalit, M., Bustard, M.T., Wright, P.C., Meeyoo, V., 2001. Novel vapor-phase biofiltration and catalytic combustion of volatile organic compounds. *Ind. Eng. Chem. Res.* 40 (23), 5334–5341.
- Li, F.B., Li, X.Z., Hou, M.F., 2004. Photocatalytic degradation of 2-mercaptobenzothiazole in aqueous La³⁺-TiO₂ suspension for odor control. *Appl. Catal. B Environ.* 48 (3), 185–194.
- Li, D.Z., Chen, Z.X., Chen, Y.L., Li, W.J., Huang, H.J., He, Y.H., et al., 2008. A New route for degradation of volatile organic compounds under visible light: Using the bifunctional photocatalyst Pt/TiO_{2-x}N_x in H₂-O₂ Atmosphere. *Environ. Sci. Technol.* 42 (6), 2130–2135.
- Li, X.Y., Zou, X.J., Qu, Z.P., Zhao, Q.D., Wang, L.Z., 2011. Photocatalytic degradation of gaseous toluene over Ag-doping TiO₂ nanotube powder prepared by anodization coupled with impregnation method. *Chemosphere* 83 (5), 674–679.
- Mo, J.H., Zhang, Y.P., Xu, Q.J., Lamson, J.J., Zhao, R.Y., 2009. Photocatalytic purification of volatile organic compounds in indoor air: a literature review. *Atmos. Environ.* 43 (14), 2229–2246.
- Mo, J.H., Zhang, Y.P., Xu, Q.J., 2013. Effect of water vapor on the by-products and decomposition rate of ppb-level toluene by photocatalytic oxidation. *Appl. Catal. B Environ.* 132–133, 212–218.

- Mondal, K., Bhattacharyya, S., Sharma, A., 2014. Photocatalytic degradation of naphthalene by electrospun mesoporous carbon-doped anatase TiO₂ nanofiber mats. *Ind. Eng. Chem. Res.* 53 (49), 18900–18909.
- Pelaez, M., Nolan, N.T., Pillai, S.C., Seery, M.K., Falaras, P., Kontos, A.G., et al., 2012. A review on the visible light active titanium dioxide photocatalysts for environmental applications. *Appl. Catal. B Environ.* 125, 331–349.
- Qu, X.G., Liu, W.X., Ma, J., Cao, W.B., 2009. Research on photodegradation of formaldehyde by nanocrystalline N-TiO₂ powders under visible light irradiation. *Res. Chem. Intermed.* 35 (3), 313–320.
- Rene, E.R., Veiga, M.C., Kennes, C., 2012. Combined biological and physicochemical waste-gas cleaning techniques. *J. Environ. Sci. Health A* 47 (7), 920–939.
- Sakai, N., Fujishima, A., Watanabe, T., Hashimoto, K., 2003. Quantitative evaluation of the photoinduced hydrophilic conversion properties of TiO₂ thin film surfaces by the reciprocal of contact angle. *J. Phys. Chem. B* 107 (4), 1028–1035.
- Soares, G.B., Bravin, B., Vaz, C.M.P., Ribeiro, C., 2011. Facile synthesis of N-doped TiO₂ nanoparticles by a modified polymeric precursor method and its photocatalytic properties. *Appl. Catal. B Environ.* 106 (3–4), 287–294.
- Sun, H.Q., Ullah, R., Chong, S., Ang, H.M., Tade, M.O., Wang, S.B., et al., 2011. Room-light-induced indoor air purification using an efficient Pt/N-TiO₂ photocatalyst. *Appl. Catal. B Environ.* 108–109 (1–2), 127–133.
- Sun, L., Cai, J.H., Wu, Q., Huang, P., Su, Y.F., Lin, C.J., 2013. N-doped TiO₂ nanotube array photoelectrode for visible-light-induced photoelectrochemical and photoelectrocatalytic activities. *Electrochim. Acta* 108, 525–531.
- Tomašić, V., Jović, F., Gomzi, Z., 2008. Photocatalytic oxidation of toluene in the gas phase: Modelling an annular photocatalytic reactor. *Catal. Today* 137 (2–4), 350–356.
- Tseng, H.H., Wei, M.C., Hsiung, S.F., Chiou, C.W., 2009. Degradation of xylene vapor over Ni-doped TiO₂ photocatalysts prepared by polyol-mediated synthesis. *Chem. Eng. J.* 150 (1), 160–167.
- Van der Meulen, T., Mattson, A., Österlund, L., 2007. A comparative study of the photocatalytic oxidation of propane on anatase, rutile, and mixed-phase anatase-rutile TiO₂ nanoparticles: Role of surface intermediates. *J. Catal.* 251 (1), 131–144.
- Vildoza, D., Ferronato, C., Sleiman, M., Chovelon, J.M., 2010. Photocatalytic treatment of indoor air: Optimization of 2-propanol removal using a response surface methodology (RSM). *Appl. Catal. B Environ.* 94 (3–4), 303–310.
- Vincent, G., Marquaire, P.M., Zahraa, O., 2009. Photocatalytic degradation of gaseous 1-propanol using an annular reactor: Kinetic modelling and pathways. *J. Hazard. Mater.* 161 (2–3), 1173–1181.
- Wang, P.H., Yap, P.S., Lim, T.T., 2011. C–N–S tridoped TiO₂ for photocatalytic degradation of tetracycline under visible-light irradiation. *Appl. Catal. A Gen.* 399 (1–2), 252–261.
- Wang, Y.Q., Jiang, X.D., Pan, C.X., 2012. “In situ” preparation of a TiO₂/Eu₂O₃ composite film upon Ti alloy substrate by micro-arc oxidation and its photo-catalytic property. *J. Alloys Compd.* 538, 16–20.
- Wei, Z.S., Sun, J.L., Xie, Z.R., Liang, M.Y., Chen, S.Z., 2010. Removal of gaseous toluene by the combination of photocatalytic oxidation under complex light irradiation of UV and visible light and biological process. *J. Hazard. Mater.* 177 (1–3), 814–821.
- Wei, X.Z., Zhu, G.F., Fang, J.F., Chen, J.Y., 2013. Synthesis, Characterization, and photocatalysis of well-dispersible phase-pure anatase TiO₂ nanoparticles. *Int. J. Photoenergy* 2013, 726872.
- Wu, D.Y., Long, M.C., Cai, W.M., Chen, C., Wu, Y.H., 2010a. Low temperature hydrothermal synthesis of N-doped TiO₂ photocatalyst with high visible-light activity. *J. Alloys Compd.* 502 (2), 289–294.
- Wu, P.G., Xie, R.C., Imlay, K., Shang, J.K., 2010b. Visible-light-induced bactericidal activity of titanium dioxide codoped with nitrogen and silver. *Environ. Sci. Technol.* 44 (18), 6992–6997.
- Yang, J., Dai, J., Li, J.T., 2011. Synthesis, characterization and degradation of Bisphenol A using Pr, N co-doped TiO₂ with highly visible light activity. *Appl. Surf. Sci.* 257 (21), 8965–8973.
- Yu, Q.L., Brouwers, H.J.H., 2009. Indoor air purification using heterogeneous photocatalytic oxidation. Part I: Experimental study. *Appl. Catal. B Environ.* 92 (3–4), 454–461.
- Yu, J.G., Wang, W.G., Cheng, B., 2012. Synthesis and enhanced photocatalytic activity of a hierarchical porous flowerlike p–n junction NiO/TiO₂ photocatalyst. *Chem. Asian. J.* 5 (12), 2499–2506.
- Yu, J.M., Liu, W., Cheng, Z.W., Jiang, Y.F., Cai, W.J., Chen, J.M., 2014. Dichloromethane removal and microbial variations in a combination of UV pretreatment and biotrickling filtration. *J. Hazard. Mater.* 268, 14–22.
- Zhang, X., Liu, Q.Q., 2008. Visible-light-induced degradation of formaldehyde over titania photocatalyst co-doped with nitrogen and nickel. *Appl. Surf. Sci.* 254 (15), 4780–4785.
- Zhang, X.T., Fujishima, A., Jin, M., Emeline, A.V., Murakami, T., 2006. Double-layered TiO₂–SiO₂ nanostructured films with self-cleaning and antireflective properties. *J. Phys. Chem. B* 110 (50), 25142–25148.
- Zhang, L.F., Sawell, S., Moralejo, C., Anderson, W.A., 2007. Heterogeneous photocatalytic decomposition of gas-phase chlorobenzene. *Appl. Catal. B Environ.* 71 (3–4), 135–142.
- Zhang, Y.Z., Xiong, X.Y., Han, Y., Zhang, X.H., Shen, F., Deng, S.H., et al., 2012. Photoelectrocatalytic degradation of recalcitrant organic pollutants using TiO₂ film electrodes: An overview. *Chemosphere* 88 (2), 145–154.
- Zhang, P.L., Yin, S., Sekino, T., Lee, S.W., Sato, T., 2013. Nb and N co-doped TiO₂ for a high-performance deNO_x photocatalyst under visible LED light irradiation. *Res. Chem. Intermed.* 39 (4), 1509–1515.
- Zhong, L.X., Haghighat, F., 2011. Modeling and validation of a photocatalytic oxidation reactor for indoor environment applications. *Chem. Eng. Sci.* 66 (23), 5945–5954.